



SGD-SST: Seamless global daily sea surface temperature products reconstruction and validation via deep spatio-temporal fusion model

Qi Wang , Qiang Zhang *, Hongjie Xie, Zifeng Liu, Yushuai Dong

Center for Hyperspectral Imaging in Remote Sensing, Information Science and Technology College, Dalian Maritime University, Dalian, 116026, China

ARTICLE INFO

Keywords:

Sea surface temperature
Seamless global daily
Deep spatio-temporal fusion model
Reconstruction
Validation

ABSTRACT

Sea Surface Temperature (SST) is a key variable in Earth's climate system. However, elements like cloud cover, aerosols, and sun glint cause substantial gaps in global daily SST products. To address this issue, this paper develops a deep spatio-temporal fusion model to reconstruct seamless global daily SST products (SGD-SST) from data collected by the Visible Infrared Imaging Radiometer Suite (VIIRS) on the Suomi National Polar-Orbiting Partnership (SNPP) Satellite. Using 9 km spatial resolution SST data from 2013 to 2024, the model generates continuous global daily SST products. In the validation experiments, this work employs three validation approaches: in-situ validation, time-series validation, and a comparison with interpolation method. The validation results demonstrate that SGD-SST products exhibit high consistency with in-situ data, with a correlation coefficient of 0.991 and a mean absolute error of 0.685. Additionally, the reconstructed missing values closely align with the original valid values in the time-series validation. Compared to interpolation method, the proposed method demonstrates better spatial continuity and reconstructing accuracy. SGD-SST products are available at <https://zenodo.org/records/14064951> and <https://zenodo.org/records/14038504>.

1. Introduction

Sea surface temperature (SST) is a critical variable in the Earth's climate system. It plays a crucial role in the interactions between the ocean and the atmosphere (Minnett et al., 2019; Pan et al., 2024). Therefore, accurate SST data is crucial for climate monitoring, weather prediction, and marine biological research (Aferskans et al., 2022; Brasnett & Colan, 2016; Xiao et al., 2019). SST observational data could be categorized into two types: the first type includes in-situ SST data based on ships, drifting buoys and moored buoys, such as the Argo buoy network dataset, in-situ sea surface temperature quality monitor (iQuam) dataset, and the International Comprehensive Ocean-Atmosphere Data Set (ICOADS) dataset (Woodruff et al., 2005; Yang et al., 2022). The second type is consist of SST products derived from remote sensing satellites. Satellite-derived SST products include those from the Visible Infrared Imaging Radiometer Suite (VIIRS) on the Suomi National Polar-Orbiting Partnership (SNPP) satellite, the Moderate Resolution Imaging Spectroradiometer (MODIS) on NASA's Terra and Aqua satellites, and the Advanced Very High Resolution Radiometer (AVHRR) on NOAA's Polar-Orbiting Environmental Satellites (POES), among others. (Kilpatrick et al., 2015; Reynolds et al., 2007).

Generally, these two types of SST data both have distinct advantages and limitations. In-situ observation data, which directly measures

oceanic environmental variables, is typically more accurate and used for the calibration and validation of SST (Kennedy, 2014). However, in-situ data is usually unevenly distributed and sparse on the global scale. It is particularly serious in remote and polar regions, where there is a lack of spatial coverage. Moreover, in-situ data requires collection using temperature instruments on specific platforms (such as ships or buoys), which needs high labor, time, and financial costs. In contrast, SST products derived from remote sensing satellites provide global spatial coverage and high-frequency observations. These products can offer long-term time-series data for SST and other climate variables, addressing the limitations of in-situ SST data on spatial coverage and temporal continuity (Lynn & Svejkovsky, 1984).

However, SST of optical remote sensing satellites are frequently missing by large gaps, primarily due to the cloud cover, aerosols and sun glint effects (Fanelli et al., 2024; Zhang et al., 2021c). Firstly, optical remote sensing satellites are always affected by cloud cover, resulting in substantial gaps in SST products at cloud-covered areas, which prevents the acquisition of complete SST data (Kabir et al., 2022; Zhang et al., 2020, 1996). Secondly, aerosols could disrupt the radiation signals received by satellite radiometers, leading to larger errors in the observation results. As a result, in regions with high aerosol concentrations, the quality of satellite data is usually poor. Even valid data may be missing (Nalli & Stowe, 2002). Finally, the sun glint effect is

* Corresponding author.

E-mail address: qzhang95@dlmu.edu.cn (Q. Zhang).

another important factor contributing to the missing SST data. Especially in high-latitude and polar regions, the reflection of sun glint could interfere with satellite radiometric measurements, resulting in errors and data loss. Consequently, the satellite-derived SST products are always incomplete with large areas of missing data (Barton, 1995; Zhang et al., 2022).

Directly using these incomplete satellite-derived SST products would significantly impact subsequent applications. In other words, the integrity of SST data directly affects the effectiveness and reliability of global climate monitoring, accurate weather forecasting, and marine biological research. Therefore, addressing the issue of missing information in SST products is a critical step before applying these products to subsequent fields.

To date, researchers have both domestically and internationally proposed various methods for reconstructing SST products. Most of the existing methods are statistical model-based approaches grounded in physical mechanisms (Aparna et al., 2018; Zhang et al., 2024). These methods mainly rely on existing SST observation data, using statistical methods and mathematical models to predict or reconstruct SST data. For example, Carton and Giese (2008) proposed the Simple Ocean Data Assimilation (SODA) method, which utilizes hydrographic profile data, ocean station data, and moored temperature and salinity observations. This method corrects the final results by assimilating the differences between the observed data and the numerical model predictions. Huang et al. (2017) developed the Extended Reconstructed Sea Surface Temperature, Version 5 (ERSST v5) products. These products utilize observational data from ships, buoys, and sea ice concentration to construct the Empirical Orthogonal Function (EOF) method (Hannachi et al., 2007). Through EOF analysis, it extracts the primary spatial and temporal variability patterns, thereby filling gaps in SST data and improving the consistency and accuracy of SST data. Additionally, Huang et al. (2021) presented the Daily Optimal Interpolation Sea Surface Temperature Version 2.0 dataset (DOISST v2.0), which is a blended dataset from ships, buoys and AVHRR satellite SST. This dataset employs an optimal interpolation method, combining data from different temporal and spatial scales to fill gaps in SST data.

However, traditional statistical model-based methods typically rely on long-term historical observational data (Kidson & Thompson, 1998). While these methods provide important SST information for ocean science, they also have several limitations (Ding et al., 2016). Traditional statistical methods usually use monthly averaged or seasonal SST data for analysis. This leads to a noticeable lag in capturing short-term fluctuations or extreme weather events. For example, monthly-scale reconstructed SST data usually fails to reflect daily oceanic thermodynamic fluctuations and the rapid interactions between the ocean and atmosphere (Haustein et al., 2016; Laurindo et al., 2022). Therefore, traditional methods exhibit poor adaptability in applications that demand high temporal resolution, such as daily or hourly data. Moreover, many traditional reconstruction methods employ low spatial resolution (such as $1^\circ \times 1^\circ$ or lower) SST data, which restricts their capacity for detailed analysis in localized marine areas (Banzon et al., 2014; Minobe & Maeda, 2005; Reynolds et al., 2007). In fields that require high spatial resolution, such as marine ecosystems, climate change monitoring, and polar research, traditional methods usually fail to provide sufficient detail, thereby impacting decision support and scientific research (Dickey et al., 2006; Hurwitz et al., 2012; Kumar et al., 2024; Oliveira e Silva

et al., 2022). Furthermore, the validation of reconstructed SST matched with in-situ data has not been fully demonstrated, making it difficult to ensure the accuracy and precision of the reconstructed SST.

To address these issues and limitations, this study firstly develops a deep spatio-temporal fusion model for the reconstruction of missing data in SST products. Next, based on this model, seamless global daily SST (SGD-SST) SNPP-VIIRS products for the period from 2013 to 2024 are generated. Finally, several validation strategies are employed to demonstrate the effectiveness and robustness of SGD-SST products. The main contributions are summarized as follows:

- A deep spatio-temporal fusion model is developed for the reconstruction of missing data in SST products. The model simultaneously considers both spatial and temporal information, incorporates the local attention mechanism through gated convolutions, and utilizes monthly average SST data to suppress the generation of anomalous values. These strategies effectively enhance the accuracy and reliability of SST reconstruction.
- Seamless global daily SST SNPP-VIIRS products (named SGD-SST) for the period from 2013 to 2024 are generated. These products include both the original and reconstructed SST data, enabling refined and comprehensive SST monitoring and analysis. SGD-SST products are available at <https://zenodo.org/records/14064951> and <https://zenodo.org/records/14038504>.
- Various validation strategies are used to demonstrate the effectiveness and robustness of SGD-SST products. The validation strategies include in-situ validation, time-series validation, and a comparison with interpolation method. The validation and comparison results show that SGD-SST products behave with high accuracy, reliability and robustness.

The remainder of this paper is organized as follows. Section 2 introduces the used data. Section 3 describes the reconstruction and validation methods. Section 4 presents the experimental results and validation comparisons. Section 5 concludes with a summary and outlook.

2. Data

2.1. SNPP-VIIRS SST Products

The SNPP satellite, equipped with the VIIRS sensor, was launched on October 28, 2011, and became operational in 2013. The VIIRS sensor represents a new era in medium-resolution imaging. It inherits the sensor technologies of AVHRR and MODIS, enabling the acquisition of high-quality global observation data, which could then be used to retrieve SST data (Minnett et al., 2014). This sensor addresses the limitations of the aging MODIS sensor and the limited record time of the AVHRR sensor. The SNPP-VIIRS sensor provides global coverage observation data twice a day, once in the morning and once in the afternoon. It has 22 bands, with a wavelength range from 0.4 to $12.5\text{ }\mu\text{m}$, including 5 visible bands and 17 medium-resolution bands. The spatial resolution of these bands is approximately 375 m and 750 m, respectively (Eplee et al., 2015; Liang & Ignatov, 2013). A detailed comparison of the key parameters of VIIRS, MODIS, and AVHRR sensors is provided in Table 1. This table highlights the advancements of VIIRS in terms of spatial resolution, swath width, cloud detection capabilities, and calibration systems, as well as its role in ensuring data continuity from earlier sensors.

Table 1
Comparison of VIIRS, MODIS, and AVHRR parameters.

Parameter	VIIRS	MODIS	AVHRR
Native resolution	375 m (I-bands), 750 m (M-bands)	1 km	1.1 km
Swath width	3000 km	2330 km	2900 km
Cloud detection bands	5 (including 0.67 μm , 0.87 μm)	3	2
Calibration system	Solar diffuser + black body	Solar diffuser + black body	Black body
Data continuity	2012-Present	2000-Present	1981-Present

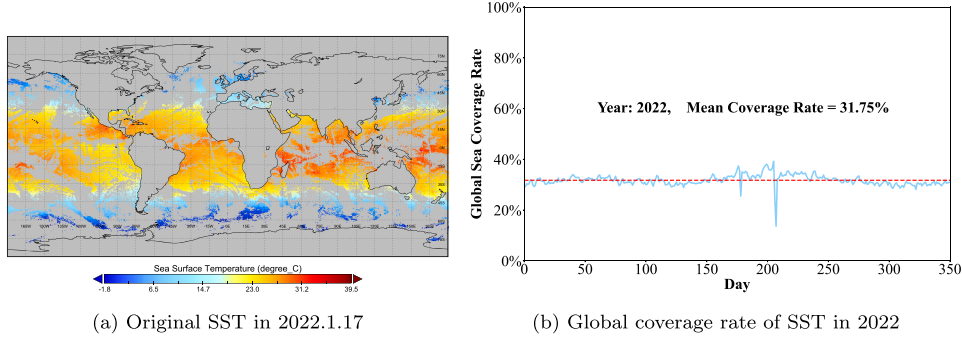


Fig. 1. The gaps and coverage rate of SNPP-VIIRS global daily SST products.

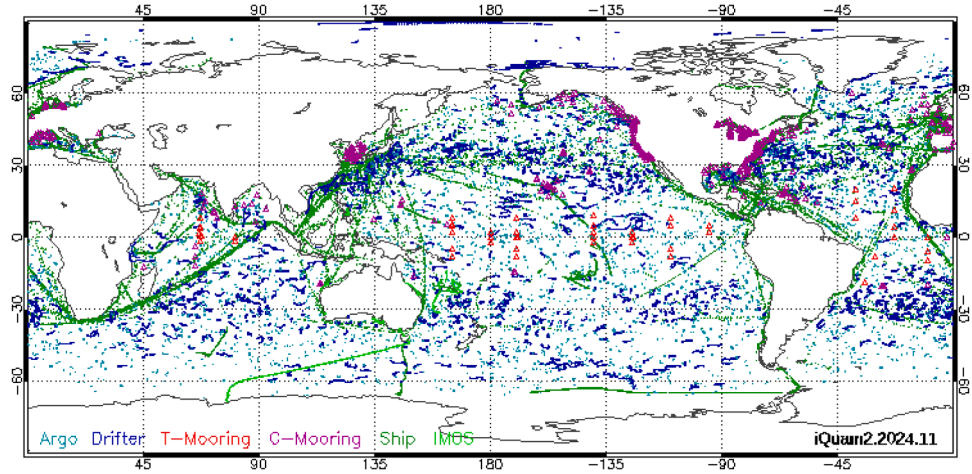


Fig. 2. In-situ data distribution of iQuam system (November 2024).

To ensure data quality, the SNPP-VIIRS uses 5 medium-resolution bands for cloud masking and SST retrieval, covering the wavelengths of $0.67\text{ }\mu\text{m}$, $0.87\text{ }\mu\text{m}$, $3.7\text{ }\mu\text{m}$, $10.7\text{ }\mu\text{m}$, and $12.0\text{ }\mu\text{m}$. SST data processing and validation are carried out by NAVO, and the retrieval algorithm employs an improved version of the Non-Linear SST (NLSST) algorithm. This algorithm has been successfully applied for MODIS and AVHRR data. During the data processing, the algorithm processes each ‘target array’, which is a small 10×6 pixel window. Cloud masking and SST retrieval are performed within a 2×2 pixel unit array, ensuring the accuracy and reliability of the results (Hillger et al., 2014; Merchant et al., 2008; Miller et al., 2013).

Our study uses the level-3 SNPP-VIIRS global daily SST products, produced and archived by the Ocean Biology Processing Group, with a spatial resolution of 9 km . The products are available at <https://oceancolor.gsfc.nasa.gov/l3/order/>. However, the products suffer from serious gaps. These gaps are especially pronounced in high-latitude regions with sea ice coverage. As shown in Fig. 1, the average coverage of the global SST products in 2022 is only 31.75 %.

2.2. Global in-situ SST data

The in-situ SST Quality Monitor (iQuam) system records SST data from observational stations. This system is designed to minimize equipment errors and environmental influences, employing stringent quality assessment standards to examine the temporal and spatial consistency, continuity, and stability of the data. In addition, the iQuam system also features real-time SST monitoring and evaluation capabilities, allowing timely feedback on the quality status of SST data. This ensures the integrity and reliability of the dataset (Sukresno et al., 2021; Zhang & Ignatov, 2021). These functionalities ensure that the iQuam system

provides high-precision and high-reliability SST data. For example, Tu et al. (2015) validated the reliability of the SST products derived from the SNPP-VIIRS via iQuam in-situ data.

As shown in Fig. 2, the SST data from the iQuam system includes observational data from multiple sources, such as Argo, Drifter, T-Mooring, and Ship. In-situ data is monthly stored, from September 1981 to the present, with the latest files continuously updated. The data quality is marked by the “quality level” field: 0-2 indicates the unusable data, while 3-5 represents low, acceptable and best quality, respectively (Xu & Ignatov, 2014; Zhang et al., 2021a).

This study uses global in-situ SST data with a quality level of 5, provided by the iQuam system. This data is used to validate the accuracy and reliability of the reconstructed SST products. The in-situ data could be downloaded from <https://www.star.nesdis.noaa.gov/socd/sst/iquam/data.html>.

3. Methodology

3.1. Reconstruction method

The flowchart of the reconstruction method in this study is depicted in Fig. 3. The reconstruction method consists of four steps. Firstly, performing data preprocessing on the missing SST products to construct the sample dataset. Secondly, constructing the deep spatio-temporal fusion model for the seamless reconstruction of global daily SST products. Thirdly, training and optimizing the deep spatio-temporal fusion model according to the corresponding loss function strategy. Finally, generate the SGD-SST products for the period 2013–2024. The detailed descriptions are given as follows.

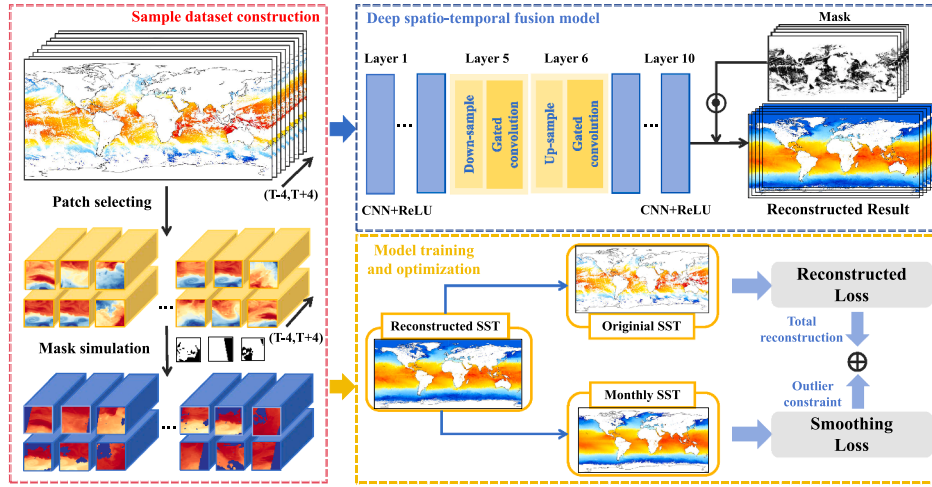


Fig. 3. Flowchart of the reconstruction method.

3.1.1. Sample dataset construction

The 9 km spatial resolution SST data from SNPP-VIIRS has the size of 2160×4320. The original data needs to be divided into small patches. Then, the corresponding labels and samples are selected to construct the sample dataset. The distribution of SST data exhibits significant seasonal variations (i.e., spring, summer, autumn and winter). Therefore, to ensure the comprehensive seasonal distribution of the samples, we select SST data from the year 2021. To improve model stability and convergence, we normalize the SST data to the range [0, 1] based on their minimum and maximum values. In this section, we select local patches with a spatial size of 40×40 and perform the global traversal of the original SST data at date T. We then calculate the number of land pixels and ocean pixels within each local patch. Then, we select local patches that contain only ocean pixels and have a missing rate of ocean pixels less than 10 % for the four preceding and four following days as labels. We then assign these selected local patches to a 3D spatio-temporal group, based on the corresponding ocean masks for the time range from date T-4 to T+4. After determining the labels, we apply the simulated masks to the local patches at date T to obtain simulated missing data, thus creating data pairs (Zhang et al., 2021b).

This study selects 8250 spatial masks from the global SNPP-VIIRS SST products for the period 2013-2024. These masks are used as simulation masks. We set the missing data rate for these masks within the range of [0.3, 0.8]. These masks randomly apply to selected local patches, simulating the complete patches with date T (label) as an incomplete local patch (data). Meanwhile, the corresponding spatio-temporal three-dimensional mask is simultaneously updated. The above process collects a total of 36,549 sample patches to construct the sample dataset. It provides training data for the subsequent deep spatio-temporal fusion model, and boosts the model's robustness for various missing types in SST data.

3.1.2. Deep spatio-temporal fusion model

As shown in Fig. 3, this work presents a deep spatio-temporal fusion model. The model simultaneously considers spatial and temporal information, incorporating the local attention mechanism through gated convolution. In addition to the conventional convolution layers, the model also includes down-sampling, up-sampling, and local attention units implemented through gated convolutions.

The deep spatio-temporal fusion model uses continuous SST data from date T-4 to T+4 days and their corresponding masks as input in Fig. 3. During the reconstruction process, the model leverages both the spatial and temporal information of the SST. Generally, in the spatial dimension, adjacent areas of SST data exhibit high spatial consistency. In the temporal dimension, SST data at the same location typically show

the high temporal correlation. It also means that, over short periods, the SST variation at the same location remains relatively stable. It is highly correlated with the temperature values at adjacent times. By combining spatial and temporal information, this work allows the model to more effectively reconstruct and predict changes in SST. In other words, the deep spatio-temporal fusion model exploits the spatial consistency and temporal correlation of SST data. This improves the accuracy and stability of the reconstruction results.

In Fig. 3, the deep spatio-temporal fusion model utilizes up-sampling and down-sampling operations to extract and fuse spatial and temporal features at different resolutions. Down-sampling reduces the data dimensions to extract global features. Up-sampling restores the data to its original resolution, ensuring the preservation of detailed information. Specifically, the down-sampling operation captures broader contextual information by lowering the data resolution. Subsequently, the up-sampling operation enables the model to reconstruct details at high resolution. In addition, the gated convolution in the deep spatio-temporal fusion model splits the feature map into two parts. One part is modified through the activation function. The other part generates gating weights using the sigmoid function. The two parts are then multiplied together (Ouyang et al., 2021; Zhan et al., 2024). This mechanism allows the model to focus on key areas, thereby improving the accuracy and reliability of the reconstruction SST data.

In summary, this work proposes a deep spatio-temporal fusion model. It effectively captures the spatial and temporal features of SST. Additionally, the model could flexibly adjust its focus regions during the reconstruction process. This improves the overall performance of the model. The combination of multi-scale feature extraction and local attention mechanism enable the model more efficiently and accurately to process SST data in complex environments.

3.1.3. Model training and optimization

After constructing the deep spatio-temporal fusion model, it is necessary to train and optimize the model. By observing the spatio-temporal distribution of global daily SST data from SNPP-VIIRS, it is uncommon to find consecutive days of missing data in the same regions. Especially in high-latitude areas covered by sea ice, SST data usually shows large gaps. In contrast, as shown in Fig. 4, the coverage of SNPP-VIIRS monthly average SST data is higher, with fewer missing areas and higher spatial consistency. Since the monthly average SST data usually does not differ much from the daily data within the same month, this work selects the monthly average data. Then this data is utilized to construct the additional loss function. It could suppress the generation of anomalous SST values, during the model training and optimization process.

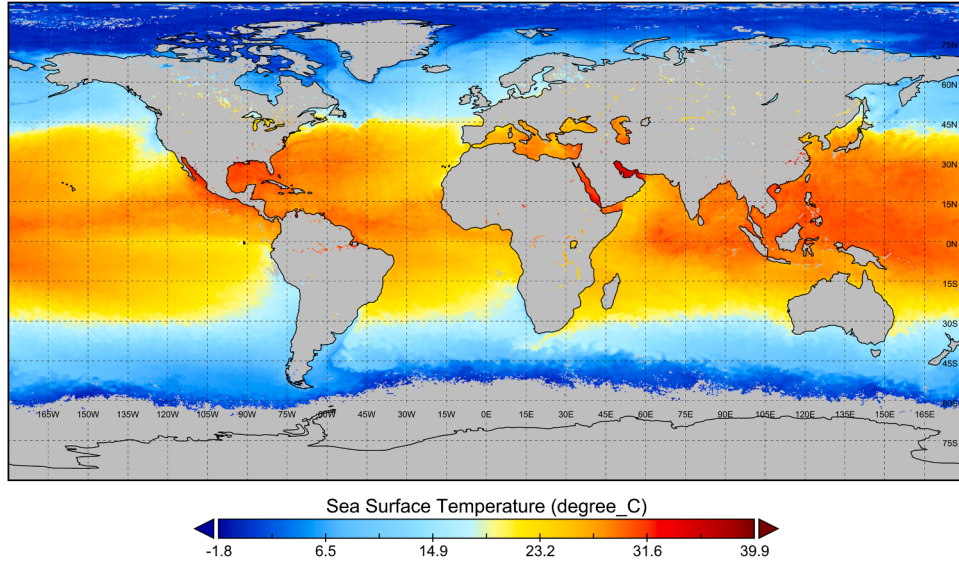


Fig. 4. SNPP-VIIRS Monthly average SST Data (August 2021).

The loss function used for model training and optimization is given in the following equations:

$$\mathcal{L}_{\text{rec}} = \frac{1}{2N} \| (1 - M_T) \odot (SST_{\text{rec}} - SST_{\text{ori}}) \|_2^2 \quad (1)$$

$$\mathcal{L}_{\text{smo}} = \frac{1}{2N} \| (1 - M_T) \odot (SST_{\text{rec}} - SST_{\text{month}}) \|_2^2 \quad (2)$$

where N represents the number of samples. M_T stands for the mask of the SST data for date T. SST_{rec} and SST_{ori} are denoted as the reconstructed SST patch and the original seamless SST patch, respectively. SST_{month} represents the monthly average SST patch. The total loss function of the deep spatio-temporal fusion model combines the reconstruction loss function \mathcal{L}_{rec} and the smoothness loss function \mathcal{L}_{smo} , as below:

$$\mathcal{L}_{\text{total}} = \mathcal{L}_{\text{rec}} + \omega \mathcal{L}_{\text{smo}} \quad (3)$$

In the reconstruction loss function, the model evaluates the difference between the reconstructed SST data and the label. This allows model to gradually approximate the real data, enabling global-scale SST reconstruction. In the smoothing loss function, the monthly average SST data are used to suppress the anomalous SST values. Both the two loss functions estimate the errors just for missing regions. It allows the deep fusion model to focus on reconstructing the missing data. The weight factor ω in the total loss function to balance \mathcal{L}_{rec} and \mathcal{L}_{smo} , is fixed at 0.1. To validate the effectiveness of the smoothing loss, we conduct an ablation study comparing the model's performance with and without this component. The results are summarized in Table 2.

The Adam algorithm is employed as the gradient descent strategy during model training and optimization. The batch size used for network training in the model is fixed at 128, with a total of 1000 epochs and an initial learning rate of 0.001. We decrease the learning rate by a decay factor of 0.5 every 100 epochs. To improve computational efficiency, we process the global SST data (2160×4320) in blocks, with each block sized 2160×1080. This strategy reduces computational complexity and

fully utilizes the parallel computing capabilities of hardware resources. Experimental results show that the model can reconstruct one day of SST data in 4.13 s and one year of SST data in approximately 50 min, demonstrating its suitability for real-time processing of large-scale marine data. For software, The proposed model utilizes the deep learning framework PyTorch. For hardware, it relies on the NVIDIA RTX 4090 GPU, i9-12900K CPU, and 64 GB RAM.

3.2. Validation method

To further validate the accuracy and effectiveness of the SGD-SST products, we employ the three following validation methods:

- a) In-situ validation: The in-situ data from the iQuam system is used as the ground truth for SST, to validate the reconstructed SST data.
- b) Temporal validation: From the temporal dimension, we evaluate whether the temporal continuity of the reconstructed SST data is consistent with that of the original SST data.
- c) A comparison with interpolation method: We compare the SGD-SST products with the traditional interpolation method, thereby validating the effectiveness of the proposed model.

It is worth noting that the in-situ validation employs a site-product spatio-temporal matching method, to assess the accuracy of the reconstructed SST data. This study uses SST in-situ data with a quality level of 5 provided by the iQuam system, covering all types of in-situ data. The specific process of the site-product spatio-temporal matching method is described as follows:

In terms of the time dimension, since the in-situ data provided by iQuam is archived as a monthly basis, the first step is to divide it into daily SST data. Next, considering that the overpass time of the SNPP satellite is 13:30 local time, the iQuam in-situ data from the time window of 12:30–14:30, is selected as the matching dataset. This ensures

Table 2
Ablation study on the effect of smoothing loss.

Metric	With smoothing loss	Without smoothing loss	Relative change
Matched points (Mean)	3,943	3,943	—
SD (Mean)	0.945	1.073	↓11.9 %
RMSE (Mean)	1.031	1.101	↓6.4 %
MAE (Mean)	0.670	0.686	↓2.3 %
R (Mean)	0.992	0.991	↑0.1 %

that the SST in-situ data is temporally aligned with the reconstructed products. Finally, invalid values in the satellite-reconstructed SST need to be removed. This process does not account for missing SST data caused by land, and only valid data from the ocean areas is retained.

In the spatial dimension, we use the iQuam in-situ data as the center and employ a KD-tree for fast searching (Hou et al., 2018). This method combines with the Haversine formula to calculate the geographic distance (McDougall et al., 2012). The spatial resolution of the SNPP-VIIRS SST data is 9-km, so a radius of 4.5-km is utilized as the matching spatial range. This strategy effectively ensures that the matching points fall within a single pixel, thereby improving the accuracy and representativeness of the matching data between the in-situ data and the reconstructed products (Xiao et al., 2014).

4. Experimental results and validation

In this section, we present the experimental results and relevant validation to demonstrate the effectiveness of SGD-SST products from January 1, 2013 to November 2, 2024. These SGD-SST products are stored in NetCDF4 format. The products could be downloaded at <https://zenodo.org/records/14064951> and <https://zenodo.org/records/14038504>.

In the experiments of this section, the performance is evaluated with standard deviation (SD, in Eq. (4)), root mean square error (RMSE, in Eq. (5)), mean absolute error (MAE, in Eq. (6)), and correlation coefficient CC (in Eq. (7)). These evaluation indexes are given as follows:

$$\sigma = \sqrt{\frac{1}{N} \sum_{i=1}^N (x_i - \bar{y})^2} \quad (4)$$

$$RMSE = \sqrt{\frac{1}{N} \sum_{i=1}^N (x_i - y_i)^2} \quad (5)$$

$$MAE = \frac{1}{N} \sum_{i=1}^N |x_i - y_i| \quad (6)$$

$$CC = \frac{\sum_{i=1}^N (x_i - \bar{x})(y_i - \bar{y})}{\sqrt{\sum_{i=1}^N (x_i - \bar{x})^2} \sqrt{\sum_{i=1}^N (y_i - \bar{y})^2}} \quad (7)$$

where N represents the number of samples. x denotes the satellite SST values. y refers to the in-situ SST values. The site-product spatio-temporal matching method described in Section 3.2 is employed to compare the accuracy of the reconstructed SST products with the original SST products.

As listed in Table 3, the average number of matching points (Num), CC, RMSE, and MAE for the original SST and SGD-SST products from 2013 to 2023 are 502,091 (1,255,865), 0.993 (0.991), 0.779 (1.073), and 0.526 (0.685), respectively. While the differences in CC, RMSE, and MAE between the original SST and SGD-SST products may seem minor at first glance, a closer examination reveals the underlying reasons.

Constrained by satellite observation conditions, the validation data of the original SST comprises 502,091 validation sites predominantly situated in cloud-free low-to-mid-latitude regions with optimal observation conditions. In these areas, sea surface temperature (SST) changes

Table 3
In-situ validation evaluation indexes for the original SST and SGD-SST products from 2013 to 2023.

SST Products	Evaluation index			
	Num	CC	RMSE	MAE
Original SST	502091	0.993	0.779	0.526
SGD-SST	1255865	0.991	1.073	0.685

gently, and observational noise is minimal, resulting in small deviations between in-situ measurements and reference values, which leads to lower RMSE and MAE values. In contrast, the SGD-SST model, designed to fill the observational gaps in the original data, expands the validation scope to high-latitude regions and complex areas with significant SST gradients, increasing the number of validation sites to 1,255,865. The intense spatio-temporal variations of SST in these newly included regions contribute to the rise in the absolute errors (RMSE/MAE) of model reconstruction.

Notably, despite the increase in RMSE and MAE, the correlation coefficient of SGD-SST remains as high as 0.991, demonstrating that the model can accurately capture the spatial distribution trend of SST even in complex environments. This consistency in trend information, coupled with the significant increase in the number of matching points, indicates a substantial improvement in spatial coverage. Overall, the SGD-SST products are generally consistent with the original SST products in terms of accuracy, ensuring the reliability of the in-situ validation method and the availability of the SGD-SST products.

4.1. Reconstruction results of SGD-SST products

As shown in Fig. 5, this section presents the global daily SST results from March 10 to 13, 2020, for both the original SST and SGD-SST products. The left column of Fig. 5 shows the incomplete original SST data, while the right column displays the reconstructed SGD-SST results.

From the spatial perspective, the reconstructed SGD-SST products in Fig. 5 maintain the spatial consistency between the missing regions and the adjacent valid regions. Especially in regions with high and low values, such as the western Pacific and the eastern Atlantic Ocean in Fig. 5, the reconstructed SGD-SST products maintain contextual continuity. Even though the original SST data has large areas of missing information, the reconstructed data remains consistent without obvious boundary effects or anomalies.

From the temporal perspective, although the original continuous daily SST results show high similarity and correlation, there are still varying degrees of differences and variations between them. The reconstructed SGD-SST results in the right column of Fig. 5 show that the proposed reconstruction model performs well on maintaining consistent time-series information, as well as on filling the specific information for different dates.

In addition, to illustrate the seasonal differences in global SST, this study also presents the reconstructed SGD-SST data for the four seasons of 2021, as shown in Fig. 6. By comparing the reconstruction SST results across different seasons, the reconstruction model demonstrates fine accuracy and reliability in various oceanic regions during each season. This further validates the robustness and applicability of the proposed model in addressing global seasonal variations.

4.2. In-situ validation

The in-situ SST data provided by iQuam could be considered as the true values of SST. After applying the site-product spatio-temporal matching procedure, it could be used to validate the SST retrieval and reconstruction results from remote sensing satellites. The details of the site-product spatio-temporal matching could be found in Section 3.2.

Fig. 7 presents the spatio-temporal matching density heatmaps between the reconstructed SGD-SST products and the in-situ iQuam SST data for the four seasons of 2018. The color intensity represents the density of matchup points. Specifically, the frequency is defined as the number of matchup points falling within the same temperature bin (i.e., the same interval on both axes). To enhance visualization across different density regions, the color scale is transformed by applying \log_{10} (actual count + 1). The horizontal axis represents the original VIIRS SST and the reconstructed SST data in missing regions, while the vertical axis represents the in-situ iQuam SST data. In Fig. 7, the red dashed line stands for the 1:1 line. Ideally, when the two datasets are perfectly consistent,

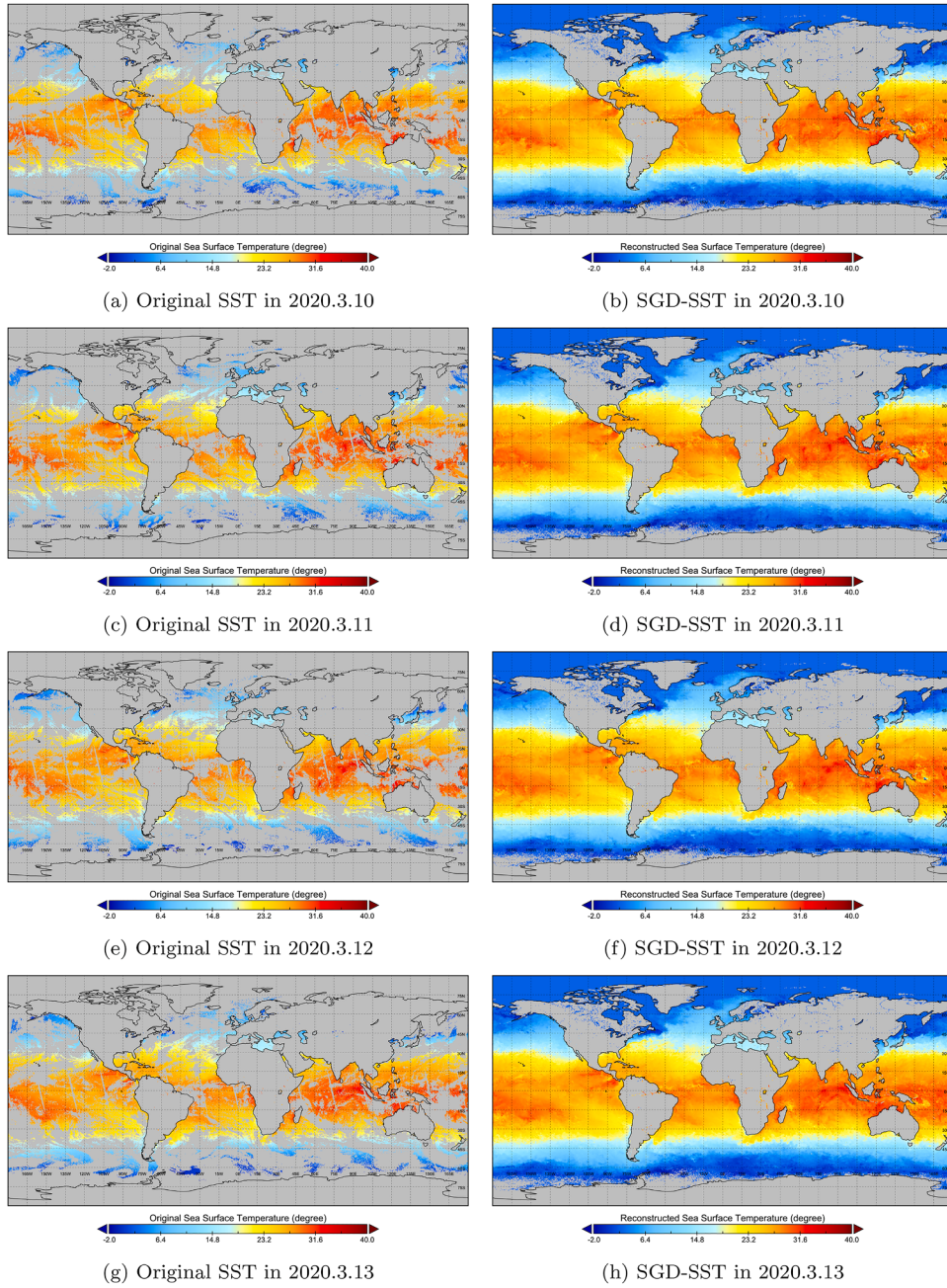


Fig. 5. Original SST and SGD-SST results from March 10 to 13, 2020.

all the points should fall on this line. The closer the points are to this line, the more consistent the VIIRS SST is with the iQuam in-situ SST. From the statistics in Fig. 7, the average number of matching points reaches 317,700. The CC value ranges between 0.985 and 0.993, indicating a high correlation between the two datasets. It also proves the high reliability of the reconstructed data. The RMSE and BIAS values range from 0.948 to 1.342 and from -0.132 to 0.023, respectively. These results indicate that the reconstructed SGD-SST products have high accuracy and reliability.

In addition, this section also displays the spatio-temporal matching scatter plots between the reconstructed SGD-SST products and the in-situ iQuam SST data for the 12 months of 2023, as shown in Fig. 8. The monthly average number of matching points is 97,192, providing a sufficient sample size for reliable statistical analysis. The CC value ranges from 0.982 to 0.994. The RMSE and BIAS values range from 0.903 to

1.296 and from 0.009 to 0.239, respectively. The relatively high RMSE value (e.g., 1.265 in June) indicates that the error of reconstructed data is slightly larger in that month. June, in summer, is more susceptible to the influence of weather systems such as monsoons and typhoons, which may lead to greater fluctuations for SST data.

In addition, increased cloud cover could affect satellite observations, leading to a larger area of missing data and thus resulting in a poorer reconstruction. Overall, although there are some fluctuations in errors in several months, the spatio-temporal matching between the reconstructed SGD-SST data and in-situ SST data is generally high. It indicates that the SGD-SST products are reliable in most cases.

As listed in Table 4, this section gives the evaluation indexes such as SD, RMSE, MAE, and CC for the SGD-SST products during the period from 2013 to 2023. Among them, the reconstruction results for 2020 and 2017 perform well across multiple indexes, indicating higher

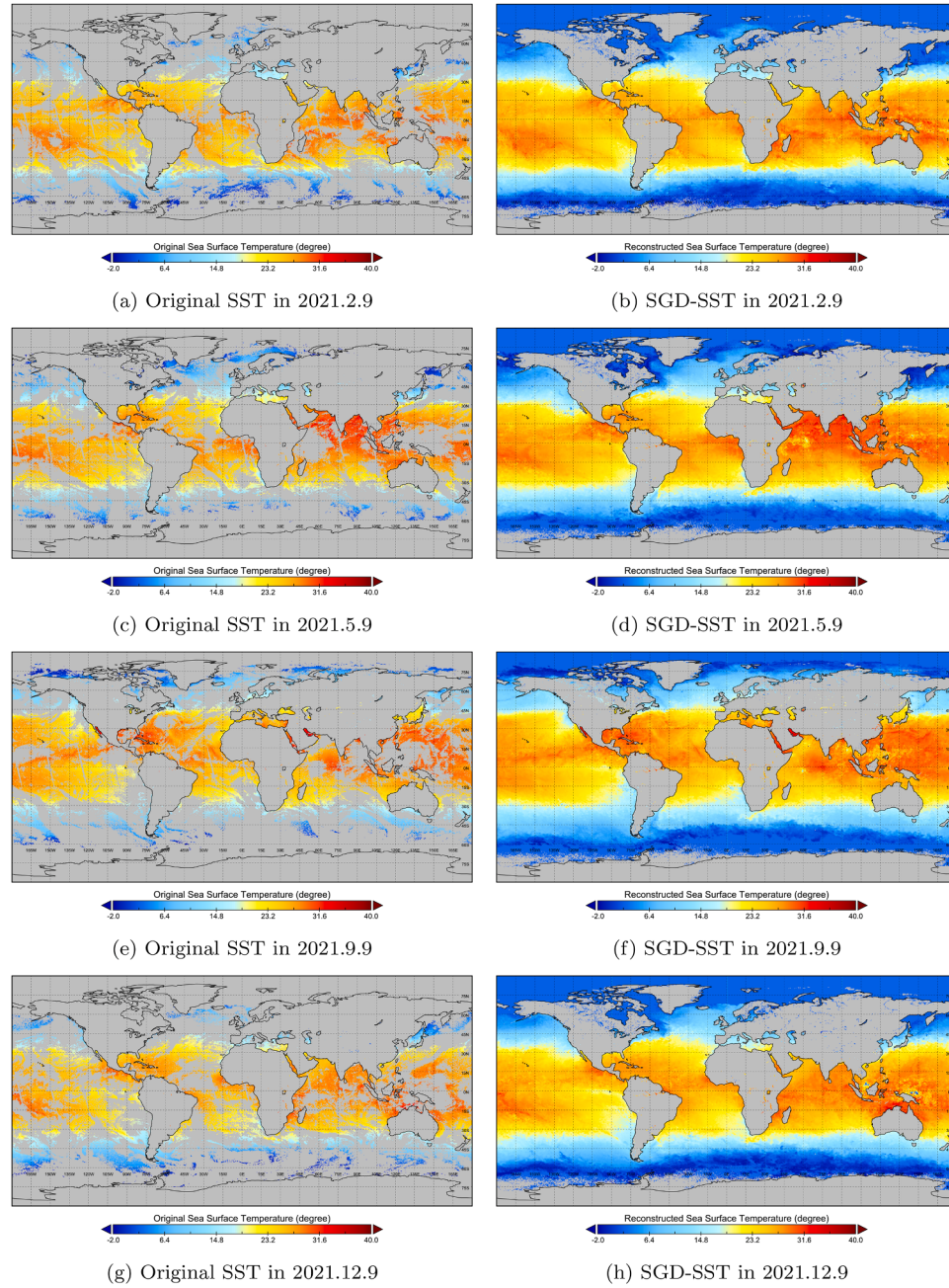


Fig. 6. Original SST and SGD-SST results for the four seasons of 2021.

reconstruction accuracy and stability for these years. Overall, the closer the correlation coefficient is to 1, the higher the consistency between the reconstructed SGD-SST data and in-situ SST data.

4.3. Temporal validation

To further validate the temporal consistency of the SGD-SST products, this subsection selects three different regions for analysis: a low-latitude region (1.71°S , 107.96°W), a mid-latitude region (34.88°S , 116.88°W), and a high-latitude region (55.71°S , 62.63°W). The continuous daily time-series variations for these three different regions are then presented as line graphs, as depicted in Fig. 9. The horizontal axis represents the continuous daily time-series values from Day 1 to Day 365 during 2023. The vertical axis stands for the SST values. In Fig. 9, the blue line represents the original SST values for the valid data, while the

Table 4
In-situ validation evaluation indexes of the SGD-SST products from 2013 to 2023.

Year	Evaluation index			
	SD	RMSE	MAE	CC
2023	1.074	1.079	0.721	0.990
2022	1.051	1.066	0.688	0.991
2021	1.025	1.032	0.680	0.992
2020	0.996	1.003	0.663	0.992
2019	1.055	1.065	0.678	0.991
2018	1.086	1.092	0.681	0.991
2017	1.020	1.025	0.662	0.992
2016	1.053	1.055	0.658	0.992
2015	1.056	1.066	0.681	0.992
2014	1.047	1.056	0.675	0.992
2013	1.061	1.068	0.688	0.991
Average	1.066	1.073	0.685	0.991

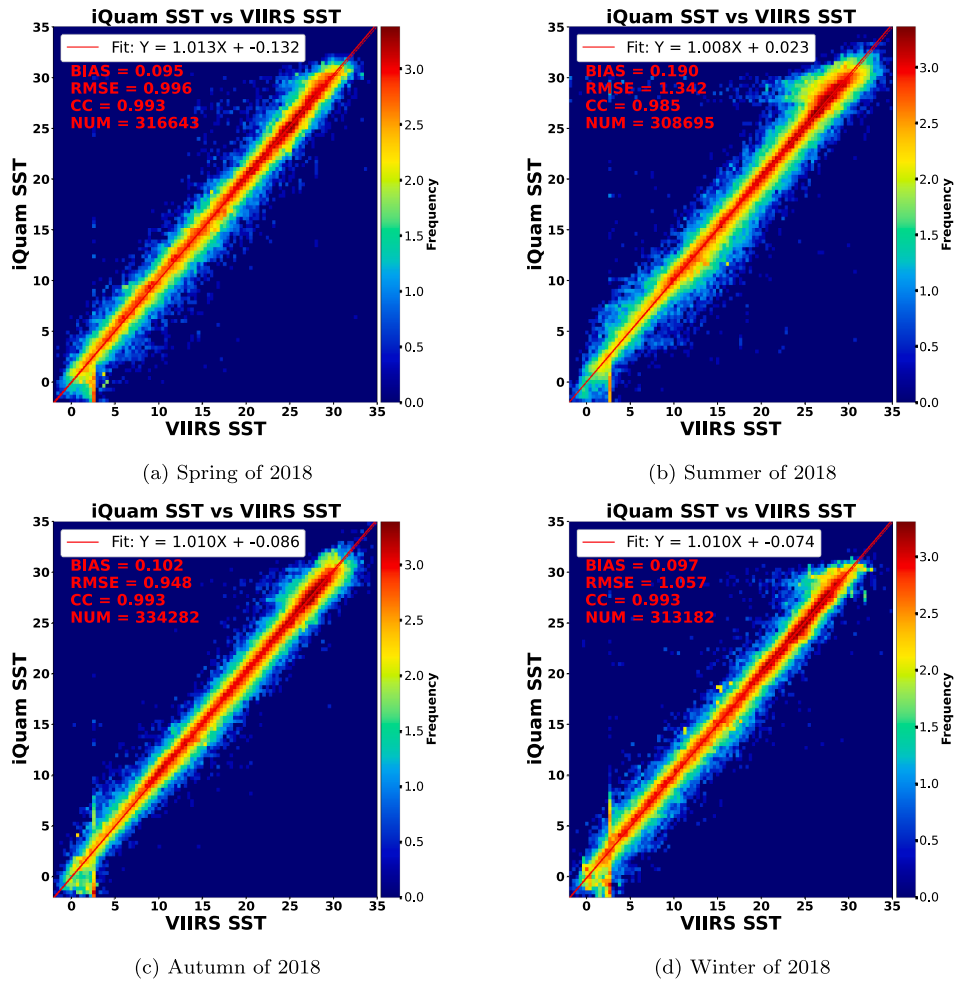


Fig. 7. Spatio-temporal matching scatter plots between the reconstructed SGD-SST products and the in-situ iQuam SST data for the four seasons of 2018.

red line represents the reconstructed SGD-SST values for the missing data.

As shown in Fig. 9, the reconstructed SGD-SST results for different ocean regions exhibit reliable temporal consistency with the original SST data. In the high-latitude region, due to cloud cover and sea ice, there is a large amount of missing data, with only 118 available days in the year. The SGD-SST products also behave satisfactory temporal consistency, as shown in Fig. 9(c). Overall, in regions with minimal missing data, the SGD-SST products are able to stably reflect temporal consistency and specificity. This temporal validation demonstrates the stability of the proposed model, as well as the usability of the SGD-SST products.

4.4. Compared with interpolation method

For the reconstructed SGD-SST products, the spatial continuity of the reconstruction results is also important. To assess the superiority of the spatial consistency of the SGD-SST products, this subsection chooses the traditional inverse distance weighting (IDW) interpolation method as the benchmark (Lu & Wong, 2008). The IDW method estimates missing values by calculating the distance between the missing pixel and its neighboring pixels, assigning higher weights to the closer valid values. In other words, this method effectively utilizes the spatial information of the SST for interpolation and reconstruction.

As shown in Fig. 10, the interpolation method tends to produce over-smoothing results, because it ignores the temporal information and does not account for areas with large spatial variance. This over-smoothing effect may lead to the loss of details, particularly in scenarios with fine

fluctuations, such as daily SST variations. In addition, in areas where SST changes significantly, such as the transition zone from mid-latitudes to high latitudes, the IDW method may lead to over-estimated SST. This is because the interpolation method may not accurately capture the actual temperature gradient in regions with rapid SST variations. In contrast, as shown in Fig. 10, SGD-SST products are superior at capturing the complex patterns and trends in the data. Therefore, SGD-SST products offer higher accuracy, better detail retention and spatial continuity.

As listed in Table 5, during the period from April 1 to 7, 2023, SGD-SST products demonstrate superior performance compared to the IDW method. The SD index of SGD-SST is lower (average of 0.882), and the average values of RMSE and MAE indexes are 0.898 and 0.632, respectively, both of which are better than the IDW values of 1.676 and 1.007. It indicates that the SGD-SST products are more stable, with smaller errors and higher accuracy. In addition, the R index of SGD-SST is 0.992, which is better than the 0.973 of the IDW method, demonstrating stronger feature learning and variability expression capability of the proposed model. Fig. 11 shows the comparison of spatio-temporal matching scatter plots at April 2, 2023, between the IDW interpolation method and SGD-SST with in-situ iQuam SST data. Clearly, compared to the IDW reconstruction results, SGD-SST products are closer to the in-situ SST data and behave fewer outliers.

Overall, IDW method relies solely on spatial information for linear interpolation, ignoring the temporal information. As a result, it struggles to capture the complex patterns in the data. The superiority of proposed model lies in its powerful feature extraction and nonlinear modeling capabilities. It could automatically learn complex spatial and temporal

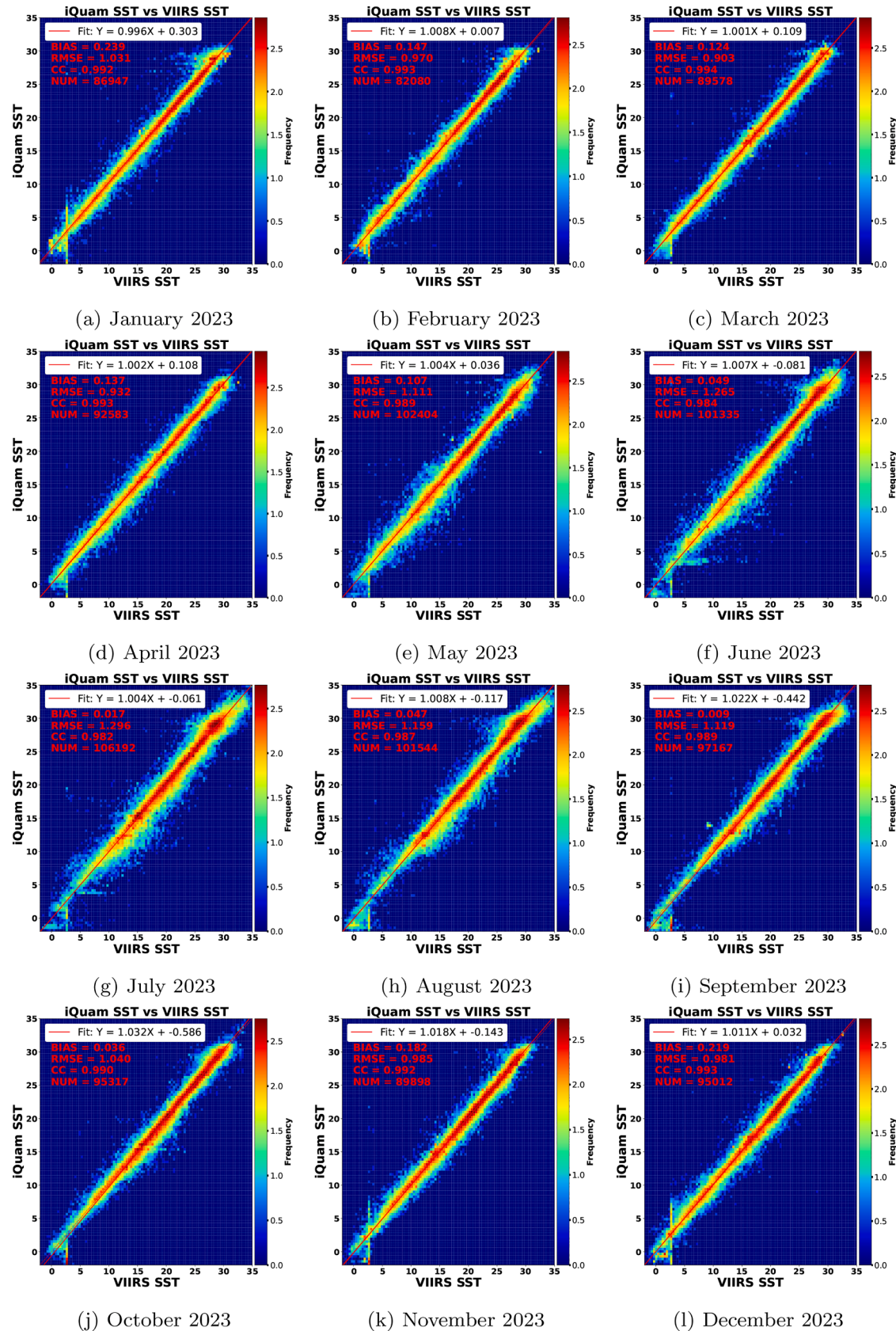


Fig. 8. Spatio-temporal matching scatter plots between the reconstructed SGD-SST products and the in-situ iQuam SST data for the 12 months of 2023.

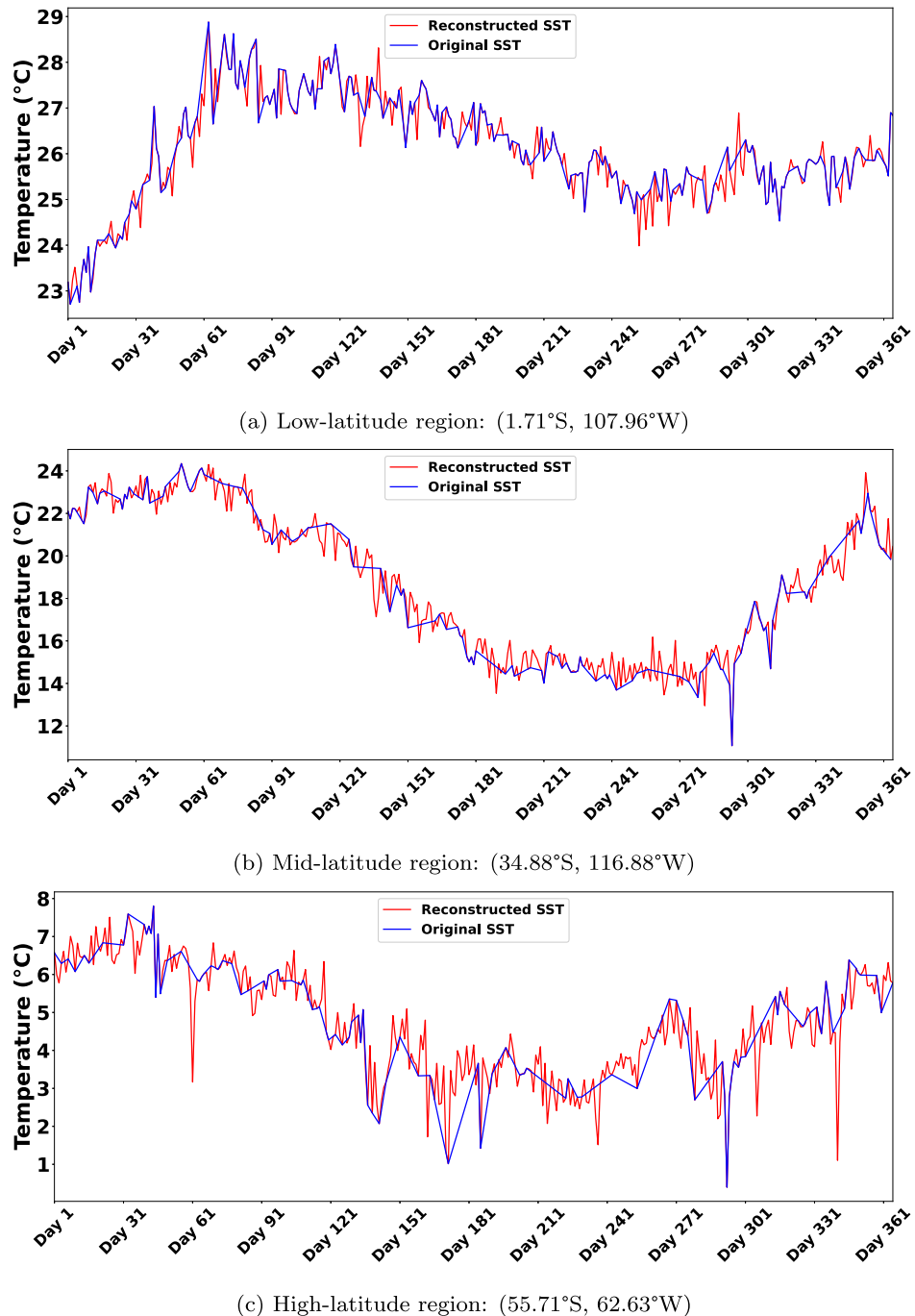


Fig. 9. Continuous daily time-series variation of the original and reconstructed SST for different regions.

Table 5

Comparison of in-situ validation evaluation indexes between the IDW interpolation method and SGD-SST products from April 1 to 7, 2023.

Index	Method	April 1	April 2	April 3	April 4	April 5	April 6	April 7	Average
SD	IDW	1.763	1.196	1.291	1.503	2.279	1.908	1.738	1.664
	SGD-SST	0.822	0.865	0.838	0.861	0.987	0.927	0.955	0.882
RMSE	IDW	1.764	1.207	1.294	1.505	2.285	1.916	1.740	1.676
	SGD-SST	0.837	0.885	0.851	0.864	0.995	0.934	0.978	0.898
MAE	IDW	0.962	0.811	0.842	0.939	1.276	1.122	1.112	1.007
	SGD-SST	0.587	0.612	0.604	0.622	0.688	0.660	0.728	0.632
CC	IDW	0.973	0.988	0.980	0.980	0.953	0.965	0.974	0.973
	SGD-SST	0.994	0.993	0.994	0.993	0.991	0.991	0.992	0.992

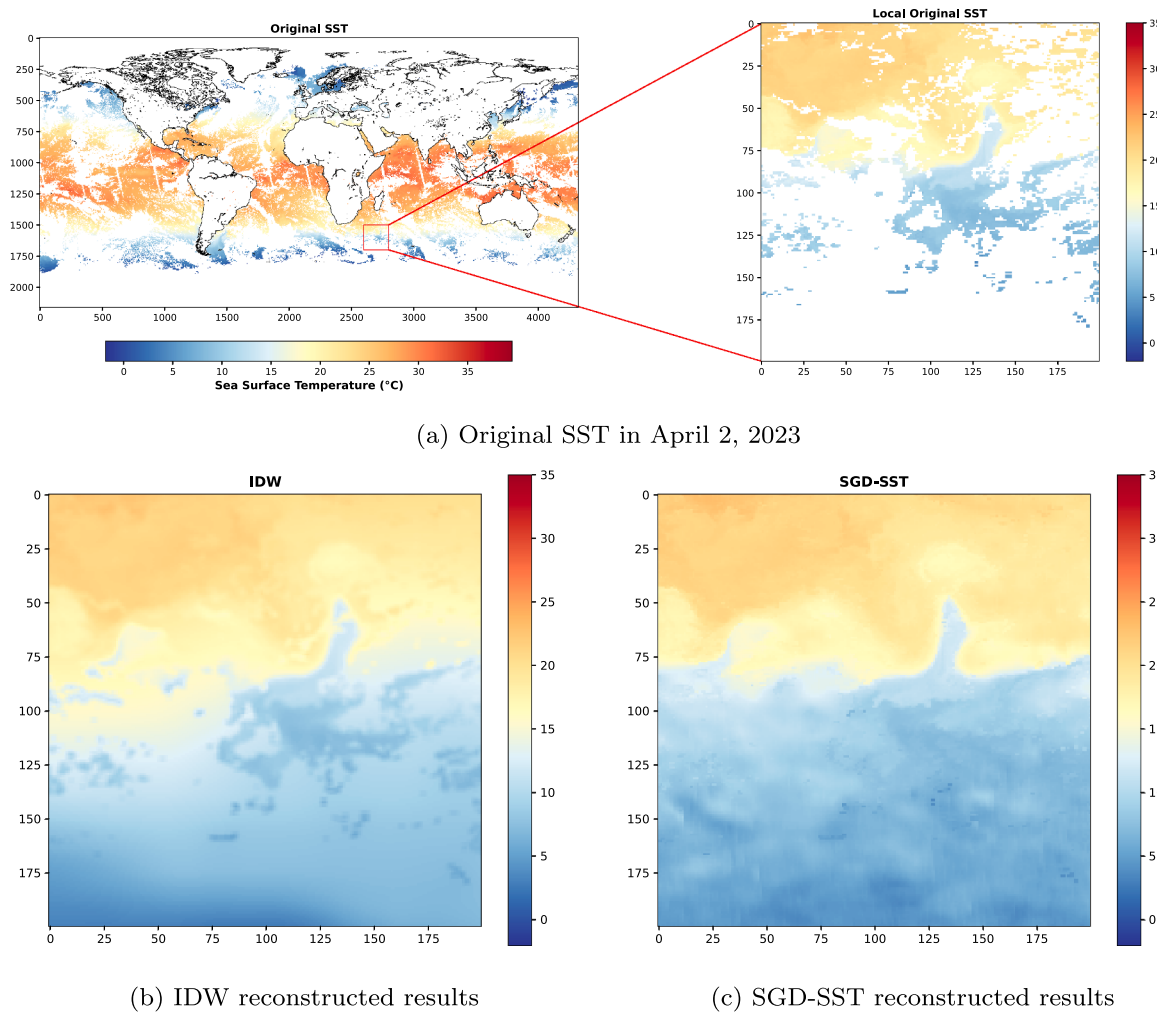


Fig. 10. Comparison of reconstructed SST results in April 2, 2023 between IDW and SGD-SST.

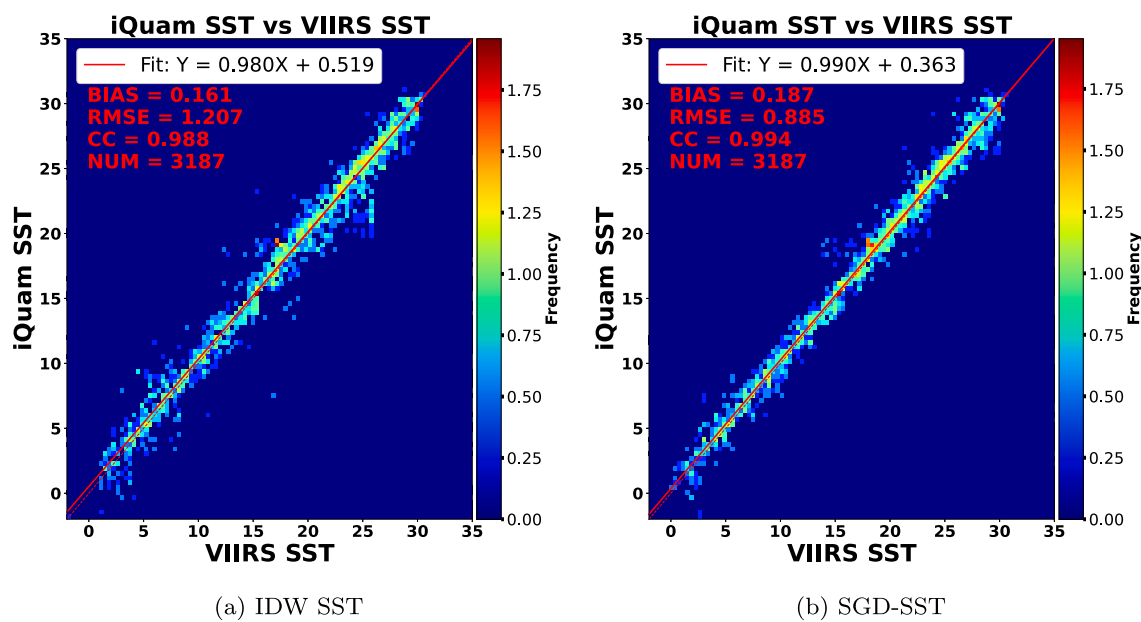


Fig. 11. Comparison of spatio-temporal matching scatter plots at April 2, 2023, between the IDW interpolation method and SGD-SST with in-situ iQuam SST data.

features, and minimize prediction errors by optimizing the loss function. This enables SGD-SST products to demonstrate greater flexibility and adaptability.

5. Conclusions

This study addresses the issue of missing information in remote sensing satellite-derived global SST data, by developing a deep spatio-temporal information fusion model. The model generates seamless global daily sea surface temperature (SGD-SST) products. Three validation methods are used to validate the accuracy and advantages of SGD-SST products: (1) in-situ validation, (2) time-series validation, and (3) a comparison with interpolation method. The validation results show that the SGD-SST products behave high accuracy, reliability and robustness.

Although the SGD-SST products perform well, there are still some shortcomings, especially that the products only use the SST data of a single source satellite. In future work, we plan to integrate SST data from multi-source satellites into the model, and introduce auxiliary data such as sea breeze for reconstruction.

CRediT authorship contribution statement

Qi Wang: Data processing, Methodology, Writing; **Qiang Zhang:** Conceptualization, Methodology, Writing; **Hongjie Xie:** Software, Reviewing; **Zifeng Liu:** Conceptualization, Writing, Validation; **Yushuai Dong:** Reviewing, Validation.

Data availability

Data will be made available on request.

Declaration of competing interest

The authors declare the following financial interests/personal relationships which may be considered as potential competing interests: Qiang Zhang reports financial support was provided by National Natural Science Foundation of China. If there are other authors, they declare that they have no known competing financial interests or personal relationships that could have appeared to influence the work reported in this paper.

Acknowledgment

This work is supported in part by the **National Natural Science Foundation of China** under Grant **62401095**; And in part by the China Postdoctoral Science Foundation under Grant **2023M740460**; And in part by the Fundamental Research Funds for the Central Universities under Grant **3132025267**; And in part by the Dalian Science and Technology Talent Innovation Supporting Project under Grant **2024RQ028**.

References

- Alerskans, E., Zinck, A. S. P., Nielsen-Englyst, P., & Hoyer, J. L. (2022). Exploring machine learning techniques to retrieve sea surface temperatures from passive microwave measurements. *Remote Sensing of Environment*, *281*, 113220.
- Aparna, S. G., D'souza, S., & Arjun, N. B. (2018). Prediction of daily sea surface temperature using artificial neural networks. *International Journal of Remote Sensing*, *39*(12), 4214–4231.
- Banzon, V. F., Reynolds, R. W., Stokes, D., & Xue, Y. (2014). A 1/4-spatial-resolution daily sea surface temperature climatology based on a blended satellite and in situ analysis. *Journal of Climate*, *27*(21), 8221–8228.
- Barton, I. J. (1995). Satellite-derived sea surface temperatures: Current status. *Journal of Geophysical Research: Oceans*, *100*(C5), 8777–8790.
- Brasnett, B., & Colan, D. S. (2016). Assimilating retrievals of sea surface temperature from VIIRS and AMSR2. *Journal of Atmospheric and Oceanic Technology*, *33*(2), 361–375.
- Carton, J. A., & Giese, B. S. (2008). A reanalysis of ocean climate using simple ocean data assimilation (SODA). *Monthly Weather Review*, *136*(8), 2999–3017.
- Dickey, T., Lewis, M., & Chang, G. (2006). Optical oceanography: Recent advances and future directions using global remote sensing and in situ observations. *Reviews of Geophysics*, *44*(1), 1–39.
- Ding, R., Li, J., Zheng, F., Feng, J., & Liu, D. (2016). Estimating the limit of decadal-scale climate predictability using observational data. *Climate Dynamics*, *46*, 1563–1580.
- Eplee, R. E., Turpie, K. R., Meister, G., Patt, F. S., Franz, B. A., & Bailey, S. W. (2015). On-orbit calibration of the Suomi National Polar-Orbiting Partnership Visible Infrared Imaging Radiometer Suite for ocean color applications. *Applied Optics*, *54*(8), 1984–2006.
- Fanelli, C., Ciani, D., Pisano, A., & Buongiorno Nardelli, B. (2024). Deep learning for the super resolution of Mediterranean sea surface temperature fields. *Ocean Science*, *20*(4), 1035–1050.
- Hannachi, A., Jolliffe, I. T., Stephenson, D. B. et al. (2007). Empirical orthogonal functions and related techniques in atmospheric science: A review. *International Journal of Climatology*, *27*(9), 1119–1152.
- Haustein, K., Otto, F., Uhe, P., Schaller, N., Allen, M. R., Hermanson, L., Christidis, N., McLean, P., & Cullen, H. (2016). Real-time extreme weather event attribution with forecast seasonal SSTs. *Environmental Research Letters*, *11*(6), 064006.
- Hillger, D., Seaman, C., Liang, C., Miller, S., Lindsey, D., & Kopp, T. (2014). Suomi NPP VIIRS imagery evaluation. *Journal of Geophysical Research: Atmospheres*, *119*(11), 6440–6455.
- Hou, W., Li, D., Xu, C., Zhang, H., & Li, T. (2018). An advanced k nearest neighbor classification algorithm based on KD-tree. In *2018 IEEE International conference on safety produce informatization (IICSPD)* (pp. 902–905). IEEE.
- Huang, B., Liu, C., Banzon, V., Freeman, E., Graham, G., Hankins, B., Smith, T., & Zhang, H. M. (2021). Improvements of the daily optimum interpolation sea surface temperature (DOISST) version 2.1. *Journal of Climate*, *34*(8), 2923–2939.
- Huang, B., Thorne, P. W., Banzon, V. F., Boyer, T., Chepurin, G., Lawrimore, J. H., Menne, M. J., Smith, T. M., Vose, R. S., & Zhang, H. M. (2017). Extended reconstructed sea surface temperature, version 5 (ERSSTv5): Upgrades, validations, and intercomparisons. *Journal of Climate*, *30*(20), 8179–8205.
- Hurwitz, M. M., Newman, P. A., & Garfinkel, C. I. (2012). On the influence of North Pacific sea surface temperature on the Arctic winter climate. *Journal of Geophysical Research: Atmospheres*, *117*(D19).
- Kabir, S., Islam, R. U., Hossain, M. S., & Andersson, K. (2022). An integrated approach of belief rule base and convolutional neural network to monitor air quality in Shanghai. *Expert Systems with Applications*, *206*, 117905.
- Kennedy, J. J. (2014). A review of uncertainty in in situ measurements and data sets of sea surface temperature. *Reviews of Geophysics*, *52*(1), 1–32.
- Kidson, J. W., & Thompson, C. S. (1998). A comparison of statistical and model-based downscaling techniques for estimating local climate variations. *Journal of Climate*, *11*(4), 735–753.
- Kilpatrick, K. A., Podestá, G., Walsh, S., Williams, E., Halliwell, V., Szczodrak, M., Brown, O. B., Minnett, P. J., & Evans, R. (2015). A decade of sea surface temperature from MODIS. *Remote Sensing of Environment*, *165*, 27–41.
- Kumar, S., Srivastava, A., & Maity, R. (2024). Modeling climate change impacts on vector-borne disease using machine learning models: Case study of Visceral leishmaniasis (Kala-azar) from Indian state of Bihar. *Expert Systems with Applications*, *237*, 121490.
- Laurindo, L. C., Small, R. J., Thompson, L., Siqueira, L., Bryan, F. O., Chang, P., Danabasoglu, G., Kamenkovich, I. V., Kirtman, B. P., Wang, H. et al. (2022). Role of ocean and atmosphere variability in scale-dependent thermodynamic air-sea interactions. *Journal of Geophysical Research: Oceans*, *127*(7), e2021JC018340.
- Liang, X., & Ignatov, A. (2013). AVHRR, MODIS, and VIIRS Radiometric stability and consistency in SST bands. *Journal of Geophysical Research: Oceans*, *118*(6), 3161–3171.
- Lu, G. Y., & Wong, D. W. (2008). An adaptive inverse-distance weighting spatial interpolation technique. *Computers & Geosciences*, *34*(9), 1044–1055.
- Lynn, R. J., & Svejkovsky, J. (1984). Remotely sensed sea surface temperature variability off California during a “Santa Ana” clearing. *Journal of Geophysical Research: Oceans*, *89*(C5), 8151–8162.
- McDougall, T. J., Jackett, D. R., Millero, F. J., Pawlowicz, R., & Barker, P. M. (2012). A global algorithm for estimating Absolute Salinity. *Ocean Science*, *8*(6), 1123–1134.
- Merchant, C. J., Le Borgne, P., Marsouin, A., & Roquet, H. (2008). Optimal estimation of sea surface temperature from split-window observations. *Remote Sensing of Environment*, *112*(5), 2469–2484.
- Miller, S. D., Straka III, W., Mills, S. P., Elvidge, C. D., Lee, T. F., Solbrig, J., Walther, A., Heidinger, A. K., & Weiss, S. C. (2013). Illuminating the capabilities of the suomi national polar-orbiting partnership (NPPO) visible infrared imaging radiometer suite (VIIRS) day/night band. *Remote Sensing*, *5*(12), 6717–6766.
- Minnett, P. J., Alvera-Azcárate, A., Chin, T. M., Corlett, G. K., Gentemann, C. L., Karagali, I., Li, X., Marsouin, A., Marullo, S., Maturi, E. et al. (2019). Half a century of satellite remote sensing of sea-surface temperature. *Remote Sensing of Environment*, *233*, 111366.
- Minnett, P. J., Evans, R. H., Podestá, G. P., & Kilpatrick, K. A. (2014). Sea-surface temperature from Suomi-NPP VIIRS: Algorithm development and uncertainty estimation. In *Ocean sensing and monitoring VI* (pp. 87–94). SPIE (vol. 9111).
- Minobe, S., & Maeda, A. (2005). A 1° monthly gridded sea-surface temperature dataset compiled from ICOADS from 1850 to 2002 and Northern Hemisphere frontal variability. *International Journal of Climatology*, *25*(7), 881–894.
- Nalli, N. R., & Stowe, L. L. (2002). Aerosol correction for remotely sensed sea surface temperatures from the National Oceanic and Atmospheric Administration advanced very high resolution radiometer. *Journal of Geophysical Research: Oceans*, *107*(C10), 36–1–36–18.
- Oliveira e Silva, L., Resende, M., Galhardas, H., Manquinho, V., & Lynce, I. (2022). Deep-Data: Machine learning in the marine ecosystems. *Expert Systems with Applications*, *206*, 117841.
- Ouyang, H., Wang, T., & Chen, Q. (2021). Internal video inpainting by implicit long-range propagation. In *Proceedings of the IEEE/CVF international conference on computer vision (ICCV)* (pp. 14579–14588).

- Pan, X., Jiang, T., Sun, W., Xie, J., Wu, P., Zhang, Z., & Cui, T. (2024). Effective attention model for global sea surface temperature prediction. *Expert Systems with Applications*, *254*, 124411.
- Reynolds, R. W., Smith, T. M., Liu, C., Chelton, D. B., Casey, K. S., & Schlax, M. G. (2007). Daily high-resolution-blended analyses for sea surface temperature. *Journal of Climate*, *20*(22), 5473–5496.
- Sukresno, B., Jatisworo, D., & Hanintyo, R. (2021). Validation of sea surface temperature from GCOM-C satellite using iQuam datasets and MUR-SST in Indonesian waters. *The Indonesian Journal of Geography*, *53*(1), 136–143.
- Tu, Q., Pan, D., & Hao, Z. (2015). Validation of S-NPP VIIRS sea surface temperature retrieved from NAVO. *Remote Sensing*, *7*(12), 17234–17245.
- Woodruff, S. D., Diaz, H. F., Worley, S. J., Reynolds, R. W., & Lubker, S. J. (2005). Early ship observational data and ICOADS. *Climatic Change*, *73*(1), 169–194.
- Xiao, C., Chen, N., Hu, C., Wang, K., Xu, Z., Cai, Y., Xu, L., Chen, Z., & Gong, J. (2019). A spatiotemporal deep learning model for sea surface temperature field prediction using time-series satellite data. *Environmental Modelling & Software*, *120*, 104502.
- Xiao, Q., Liu, Y., Kondragunta, S., & Zhang, H. (2014). Evaluation of VIIRS, GOCE, and MODIS Collection 6 AOD retrievals against ground sunphotometer measurements over East Asia. In *Agu fall meeting abstracts* (pp. A111–3109). (vol. 2014).
- Xu, F., & Ignatov, A. (2014). In situ SST quality monitor (iQuam). *Journal of Atmospheric and Oceanic Technology*, *31*(1), 164–180.
- Yang, Y. C., Lu, C. Y., Huang, S. J., Yang, T. Z., Chang, Y. C., & Ho, C. R. (2022). On the reconstruction of missing sea surface temperature data from Himawari-8 in adjacent waters of Taiwan using DINEOF conducted with 25-h data. *Remote Sensing*, *14*(12), 2818.
- Zhan, S., Cai, Y., Xiu, C., Zuo, D., Wang, D., & Chun Wong, S. (2024). Parallel framework of a multi-graph convolutional network and gated recurrent unit for spatial-temporal metro passenger flow prediction. *Expert Systems with Applications*, *251*, 123982.
- Zhang, H., & Ignatov, A. (2021). A completeness and complementarity analysis of the data sources in the NOAA in situ sea surface temperature quality monitor (iQuam) system. *Remote Sensing*, *13*(18), 3741.
- Zhang, H., Ignatov, A., & Hinshaw, D. (2021a). Evaluation of the in situ sea surface temperature quality control in the NOAA in situ SST quality monitor (iQuam) system. *Journal of Atmospheric and Oceanic Technology*, *38*(7), 1249–1263.
- Zhang, Q., Yuan, Q., Li, J., Li, Z., Shen, H., & Zhang, L. (2020). Thick cloud and cloud shadow removal in multitemporal imagery using progressively spatio-temporal patch group deep learning. *ISPRS Journal of Photogrammetry and Remote Sensing*, *162*, 148–160.
- Zhang, Q., Yuan, Q., Li, J., Wang, Y., Sun, F., & Zhang, L. (2021b). Generating seamless global daily AMSR2 soil moisture (SGD-SM) long-term products for the years 2013–2019. *Earth System Science Data*, *13*(3), 1385–1401.
- Zhang, Q., Yuan, Q., Li, Z., Sun, F., & Zhang, L. (2021c). Combined deep prior with low-rank tensor SVD for thick cloud removal in multitemporal images. *ISPRS Journal of Photogrammetry and Remote Sensing*, *177*, 161–173.
- Zhang, Q., Yuan, Q., Song, M., Yu, H., & Zhang, L. (2022). Cooperated spectral low-rankness prior and deep spatial prior for HSI unsupervised denoising. *IEEE Transactions on Image Processing*, *31*, 6356–6368.
- Zhang, Q., Zheng, Y., Yuan, Q., Song, M., Yu, H., & Xiao, Y. (2024). Hyperspectral image denoising: From model-driven, data-driven, to model-data-driven. *IEEE Transactions on Neural Networks and Learning Systems*, *35*(10), 13143–13163.
- Zhang, T., Stamnes, K., & Bowling, S. A. (1996). Impact of clouds on surface radiative fluxes and snowmelt in the Arctic and subarctic. *Journal of Climate*, *9*(9), 2110–2123.